Effect of Elongational Viscosity on Axisymmetric Entrance Flow of Polymers

MAHESH GUPTA

Department of Mechanical Engineering-Engineering Mechanics
Michigan Technological University
Houghton, Michigan 49931

A finite element simulation of the flow in a channel with an abrupt contraction is presented. The effects of the shear and elongational viscosities of a polymer on the entrance flow are analyzed employing a truncated power-law model. The power-law index and the strain rate characterizing the transition from Newtonian to power-law behavior for the elongational viscosity are treated as being independent of the values of these two parameters for the shear viscosity. The effect of flow rate on entrance flow is also analyzed. It is confirmed that the Trouton ratio is important in determining the recirculating vortex and the extra pressure loss in entrance flow. Extra pressure loss and vortex length predicted by a finite element simulation of entrance loss are compared with the corresponding predictions from Binding's approximate analysis.

INTRODUCTION

In contrast to low molecular weight fluids, which can be characterized by the Newtonian constitutive equation, polymeric fluids exhibit complex rheological behavior such as strain-rate-dependent shear viscosity, high resistance to elongational deformation, normal stresses in shear flow and memory of its previous configurations during a deformation (1). Depending upon the type of flow, different constitutive approaches have been used in the literature to model the rheology of polymers. For instance, in many applications involving shear-dominated flows, such as injection molding, a generalized Newtonian constitutive equation with shear-thinning viscosity has been successfully employed (2–4). However, in applications involving elongational flow, such as extrusion dies, predictions from a generalized Newtonian formulation can be quite different from the real polymeric flow. Therefore, use of a constitutive equation which can predict shear as well as elongational viscosity is required for an accurate simulation of such flows. To alleviate the limitations of generalized Newtonian models, many different viscoelastic constitutive equations have been proposed in the literature (5). Even though many of the viscoelastic constitutive equations can qualitatively predict the phenomena such as die swell and recirculation during creeping flow in a channel with abrupt contraction, the predictions from these equations are not always in good quantitative agreement with the corresponding experimental data (6–14). Furthermore, use of a viscoelastic constitutive equation requires the values of various parameters such as relaxation time and viscosity for various modes in the constitutive equation. Since experimental determination of elongational viscosity is difficult at high strain rates, various parameters in a viscoelastic constitutive equation are often determined by fitting the viscosity and normal stress coefficient vs. strain rate data in a shear flow. However, if the viscoelastic parameters are determined by fitting only the shear properties, the constitutive equation may not accurately predict the elongational behavior of the polymer. Moreover, most of the numerical schemes for simulating viscoelastic flows fail to converge at high strain rates. Even though significant progress has been made in the last decade towards identification of underlying causes for divergence of simulation and towards development of stable numerical schemes, convergence of a viscoelastic flow simulation is still not guaranteed. Because of these difficulties, viscoelastic flow simulation of polymeric flows is rarely employed to resolve industrial problems.

In the present work, a software for simulation of axisymmetric polymeric flows has been developed. Besides shear viscosity, this software requires a knowledge of the strain-rate dependence of the elongational viscosity of the polymer. In applications involving significant elongational flow, this software can accurately predict the velocity and pressure fields in the flow. However, the constitutive equation employed in the software does not predict normal stresses in shear flow. Therefore, if normal stresses in shear flow are important to capture the physics of the problem of interest, such as die swell, predictions from this software may not be very accurate. This paper uses the

newly developed software to analyze the effect of elongational viscosity on the recirculating vortices and pressure drop in an axisymmetric channel with abrupt contraction. Corresponding software packages for planar and three-dimensional polymeric flows, which are being currently developed, will be reported in the near future.

SHEAR AND ELONGATIONAL VISCOSITIES OF A POLYMER

For axisymmetric flow, the shear and elongational viscosities are defined respectively as follows:

$$\tau_{rz} = \eta_s \dot{\gamma} \tag{1}$$

$$\tau_{zz} - \tau_{rr} = \eta_e \dot{\varepsilon} \tag{2}$$

where $\tau_{..}$ denotes various components of the stress tensor, η_s and η_e are, respectively, the shear and elongational viscosities, with $\dot{\gamma}$ and $\dot{\varepsilon}$ being the corresponding strain rates.

The shear and elongational viscosities of a Newtonian fluid are constant. For an axisymmetric flow of a Newtonian fluid, the Trouton ratio ($Tr \equiv \eta_e/\eta_s$) is 3. For polymers, shear and elongational viscosities depend upon strain rate. At low values of strain rate, the shear and elongational viscosities of a polymer are typically constant. For axisymmetric flow, the Trouton ratio for the zero-strain-rate shear and elongational viscosities of a polymer is generally 3. As the strain rate is increased beyond the Newtonian limit, the shear viscosity of a polymer decreases with increasing strain rate, whereas the elongational viscosity may actually increase followed by a decrease as the strain rate is further increased. This is illustrated for LDPE by the results from Luan and Schuch (15), reproduced in *Fig. 1*. For HDPE and polystyrene, the initial increase in the elongational viscosity beyond the Newtonian limit was not observed (16–18), whereas for polyisobutylene-isoperene copolymer the elongational viscosity has been found to be a constant independent of strain rate (19). More complex behavior, such as a second increase in elongational viscosity beyond the strain-thinning region, has also been observed for some polymers (20).

For generalized Newtonian fluids, the shear viscosity is represented as a function of the second invariant of the strain rate tensor:

$$\eta_s = \eta_s(e_{II})$$

where $e_{II} = \sqrt{2(\tilde{e}:\tilde{e})}$, $\tilde{e} = (\nabla\hat{v} + \nabla\hat{v}^T)/2$ is the strain-rate tensor and $\hat{v}$ is the velocity vector. In the present work, elongational viscosity has also been represented as a function of e_{II} as defined above. It should be noted that for simple shear flow, $e_{II} = \dot{\gamma}$, whereas for axisymmetric elongational flow, $e_{II} = \sqrt{3}\,\dot{\varepsilon}$. In the literature, η_e is generally specified as a function of $\dot{\varepsilon}$ and not that of e_{II}. However, if η_s, as well as η_e, are both specified as functions of e_{II}, it can be easily shown that, irrespective of the strain rate, $\eta_e = 3\eta_s$ for axisymmetric flow of all generalized Newtonian fluids.

Instead of focussing on a specific polymer, the goal of this paper is to examine the effect of elongational viscosity on entrance flow. As shown in *Fig. 2*, the shear as well as elongational viscosities have been represented by the truncated power-law model:

$$\eta_s = Ae_{II}^{n-1} \text{ for } e_{II} > e_0, \quad \eta_s = \eta_0 \text{ for } e_{II} \le e_0 \tag{3}$$

and

$$\eta_e = Be_{II}^{m-1} \text{ for } e_{II} > e_1, \quad \eta_e = 3\eta_0 \text{ for } e_{II} \le e_1. \tag{4}$$

However, the power-law indices as well as the strain rates for transition from Newtonian to power-law behavior can be different for the shear and elongational viscosities. Power-law model has been used by many authors in the recent literature (21–29) to represent the shear and elongational viscosities of polymers. Elongational viscosity for many polymers such as HDPE (16, 17) and polystyrene (18) can be accurately

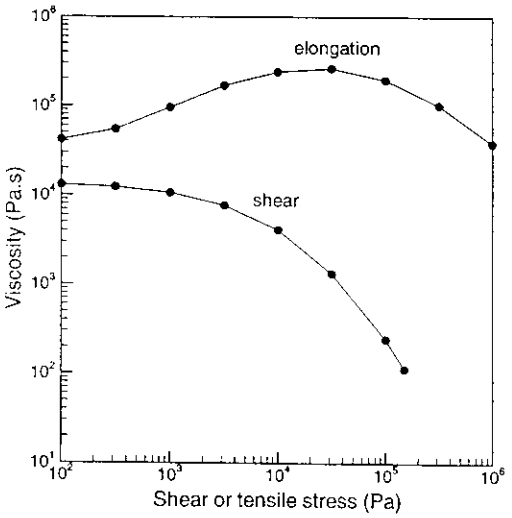

Fig. 1. Shear and elongational viscosities of LDPE6 (15).

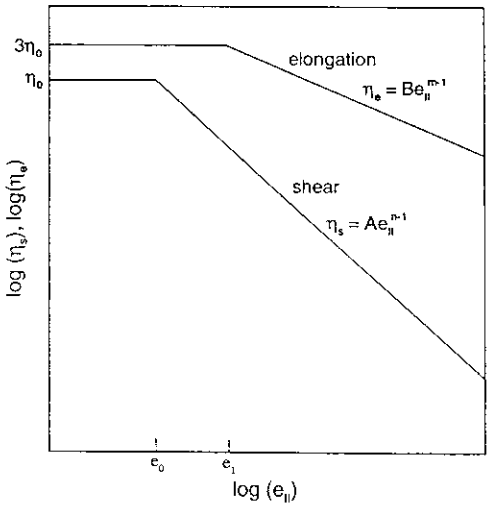

Fig. 2. Truncated power-law model for shear and elongational viscosities.

represented by a truncated power-law model. However, the initial increase in elongational viscosity beyond the Newtonian region, which is exhibited by some polymers such as LDPE (15), cannot be addressed by the truncated power-law model. Because of its simplicity, and feasibility of separating the effects of elongational viscosity parameters m and e_1 on polymeric flows, the truncated power-law model has been used in the present work. However, our software can be used with any other model specifying the strain-rate dependence of shear and elongational viscosities. It is noted that for $m = n$ and $e_0 = e_1$, the model given by *Eqs 3* and *4* is identical to a purely viscous generalized Newtonian formulation for a truncated power-law model with power-law index and Newtonian limit of n and e_0, respectively. The effect of power-law index (m) and that of the Newtonian limit (e_1) for elongational viscosity on entrance flow are analyzed later in the paper. For constant shear and elongational viscosity parameters, the effect of flow rate on entrance flow is also analyzed.

ENTRANCE FLOW

The flow near an abrupt contraction in a channel (entrance flow) is highly extension dominated. Therefore, entrance flow is a good benchmark test for analyzing the effect of elongational viscosity on polymeric flows. Besides being a good test case, entrance flow is often encountered in polymer-processing applications, such as extrusion dies and the runners in injection molding. Axisymmetric entrance flow of polymers as well as that of Newtonian fluids has been investigated extensively in the literature. For Newtonian fluids it has been established experimentally and by numerical simulation that the main cause of a recirculating vortex near the abrupt contraction is the fluid inertia. In contrast, for creeping flow of polymers, it has been experimentally demonstrated by many researchers that a recirculating vortex is found near the abrupt contraction, which can grow significantly with the flow rate in the channel (30–33). Furthermore, at certain flow rates, experiments have shown the formation of a second vortex, called lip vortex, near the entrant corner. In comparison with axisymmetric flow, a weaker vortex enhancement is found for planar entrance flow and formation of a lip vortex is rare (34–36). Only axisymmetric entrance flow has been analyzed in this paper. Similar investigation of a planar entrance flow will be presented in the near future.

Since the flow near an abrupt contraction is highly extension dominated, in addition to the pressure drop for fully developed flow in the upstream and downstream channels, an extra pressure loss is encountered in the entrance flow. Because of the high elongational viscosity of polymers, this extra pressure loss, called the entrance loss, can be particularly large for polymers. A good review on the effect of elongational properties of a polymer on entrance flow can be found in White *et al.* (31). By separately calculating the pressure drop due to shear and elongational flow near an abrupt contraction, Cogswell (21) developed analytical expressions for an approximate calculation of entrance loss in a fluid with different power-law indices for shear and elongational viscosities. Such approximate expressions for entrance loss have been further refined in the recent literature by other researchers (22–27). In particular, Binding (25) employed energy principles to relate the entrance loss and vortex length in an entrance flow to the flow rate and the shear and elongational viscosities of polymer. Binding used independent power-law models to represent the shear and elongational viscosities. However, for sake of mathematical simplicity, the power-law models were not truncated at the lower strain rates. Therefore, at low strain rates, Trouton ratio may not be 3 in Binding's analysis. Ignoring this minor difference in the two rheological models, later in this section, for a 4:1 entrance flow, the extra pressure loss and vortex length predicted by a finite element simulation with the truncated power-law model for shear and elongational viscosities are compared with the corresponding values computed by using the analytical expressions developed by Binding (25).

Instead of an approximate calculation of entrance loss, in the present work the effect of shear and elongational viscosities of polymeric fluids has been accurately captured in the constitutive equation used for the flow simulation. Even though in this paper the present finite-element software has been used solely to simulate a 4:1 entrance flow, the constitutive theory employed is frame invariant and the software is capable of simulating any complex axisymmetric polymeric flow. The effects of flow rate and elongational viscosity on entrance loss are analyzed later in this paper. The entrance loss is expressed in terms of an equivalent length of the downstream channel:

$$L_e = \frac{\Delta p - \Delta p_1 - \Delta p_2}{\partial p_2} \tag{5}$$

where Δp is the total pressure drop in the entrance flow, Δp_1 and Δp_2 are, respectively, the pressure drop for fully developed flow in the portions of the channel upstream and downstream of the abrupt contraction, and ∂p_2 is the magnitude of the fully developed axial pressure gradient in the downstream channel. The Trouton ratio for the strain rate at the down stream wall has been used to characterize the flow. The finite-element simulations presented later in the paper show that the Trouton ratio plays an important role in determining the recirculating vortex and extra pressure loss in entrance flow.

Convergence With Mesh Refinement

To check the convergence of the numerical simulation, a 4:1 axisymmetric entrance flow was simulated by three successively refined finite element meshes shown in *Fig. 3*. The lengths of the upstream and downstream channels have been taken as $20R_2$ and $30R_2$, respectively, where R_2 is the radius of the downstream channel. Along with the symmetry condition

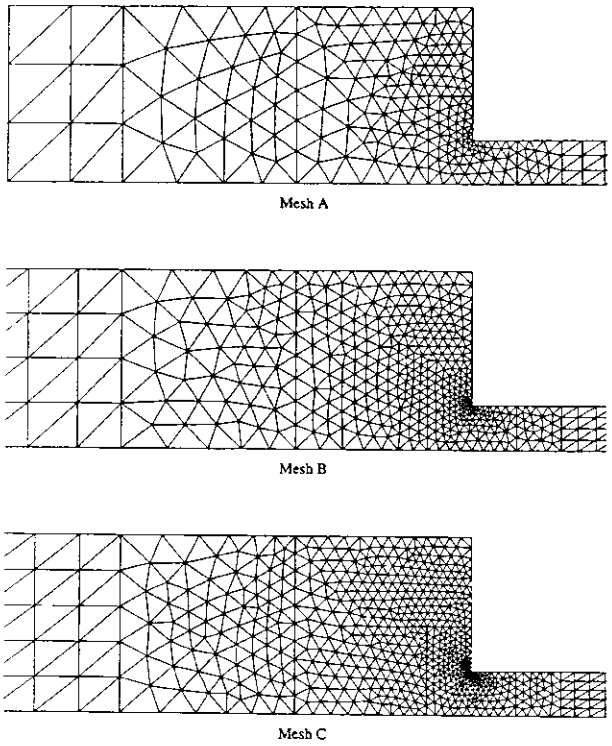

Fig. 3. Successively refined finite-element meshes used for simulating 4:1 axisymmetric entrance flow. In terms of the radius of the downstream channel, R_2, the length of the upstream and downstream channels are $20R_2$ and $30R_2$, respectively. Beyond the portion of the flow domain shown, the finite-element length along the flow direction continues to increase in the upstream and downstream sections in the three meshes.

along the axis and no-slip condition along the wall, a fully developed flow was specified at the entrance and the exit. For the three successively refined meshes, *Figs. 4* and *5* show the velocity and pressure along the axis of symmetry for power-law indices $n = 0.25$, $m = 0.5$, Newtonian limits $e_0 = e_1 = 0.001\ s^{-1}$ and for the average strain rate in the downstream channel $\dot{\gamma}_{av} = U/R_2 = 1 s^{-1}$, where U is the average velocity in the downstream channel. In *Figs. 4* and *5*, $z/R_2 = 0$ corresponds to the abrupt contraction. Away from the abrupt contraction, the velocity and pressure predicted by meshes B and C are almost identical, confirming the convergence with respect to mesh refinement. Mesh C has been used for all the flow simulations presented later in this paper. Near the abrupt contraction in *Fig. 5*, the pressure along the center line shows some fluctuations, which diminish as the mesh is refined. The center-line velocity in *Fig. 4* shows a kink at the abrupt contraction. Beyond the kink at the abrupt contraction, the center-line velocity increases monotonously to approach the value for a fully developed flow in the downstream channel. It is noted that the predicted development of center-line velocity in *Fig. 4* is quite different from the velocity development predicted by the viscoelastic flow simulations reported in the literature. Such simulations predict an overshoot in the center-line velocity near the abrupt contraction, before it decreases to its value for a fully developed flow (7–14). Since most viscoelastic constitutive equations include the effect of high elongational viscosity as well as that of the normal stresses in a shear flow of polymers, whereas the current work does not capture the normal stresses in a shear flow, a difference between the development of center-line velocity predicted in the present work and the development predicted by viscoelastic flow simulations in the literature is not completely unexpected. However, in comparison with viscoelastic flow simulations, a much weaker overshoot in center-line velocity has been observed in the experimental work reported in the literature. For instance, Azaiez *et al.* (37) found that for flow of a polymer solution their center-line velocity prediction based upon a viscoelastic flow simulation indicated a much larger overshoot than the

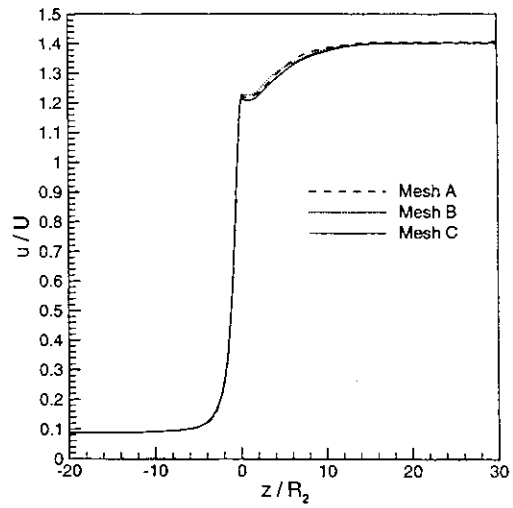

Fig. 4. Velocity along the axis of symmetry for $n = 0.25$, $m = 0.7$, $e_0 = e_1 = 0.001\ s^{-1}$ and $\dot{\gamma}_{av} = 1\ s^{-1}$.

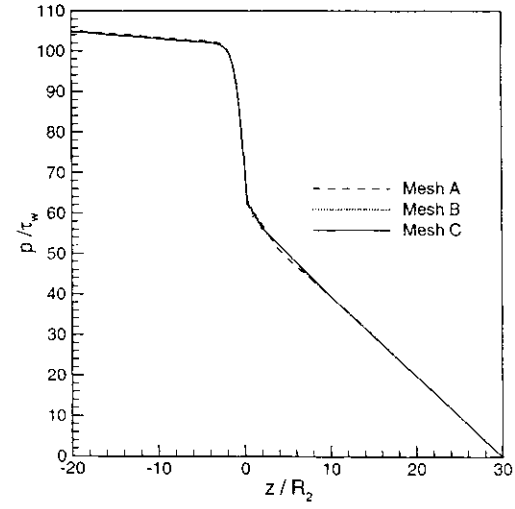

Fig. 5. Pressure along the axis of symmetry for $n = 0.25$, $m = 0.7$, $e_0 = e_1 = 0.001\ s^{-1}$ and $\dot{\gamma}_{av} = 1\ s^{-1}$.

corresponding experimental results of Quinzani *et al.* (38). Also, the velocity overshoot predicted by viscoelastic flow simulation increases with flow rate (37), whereas the velocity overshoot in the experimental data of Quinzani *et al.* (38) seems to decrease with flow rate.

Effect of Elongational Power-Law Index on Entrance Flow

With the flow rate, Newtonian limits for the shear and elongational viscosities, and power-lax index for shear viscosity being constant ($\dot{\gamma}_{av} = 1s^{-1}$, $n = 0.25$, $e_0 = e_1 = 0.001s^{-1}$), *Fig. 6* shows the effect of elongational power-law index (m) on recirculating vortex in an axisymmetric 4:1 entrance flow. To depict the flow direction, *Fig. 6* shows the unit vectors along the direction of velocity. It should be noted that near the center of circulation of a vortex, or any other stagnation point, if the predicted velocity has the same order of magnitude as the computational error, the direction shown by the unit vectors in *Fig. 6* may not be very accurate. For $m = 0.25$, which corresponds to a purely viscous generalized Newtonian formulation for the truncated power-law model with $n = 0.25$, in *Fig. 6 (a)* no significant recirculating vortex is formed near the abrupt contraction. As the elongational power-law index is increased to $m = 0.5$ (*Fig. 6 (b)*), a small recirculating vortex is formed near the outside corner. It is noted that two of the unit vectors near the entrant corner are in the upstream direction. This indicates that a lip vortex is about to form and the flow is almost stagnant near the two spurious unit vectors. For $m = 0.5$, the magnitude of the normalized velocity, where the normalization is with respect to the average velocity in the downstream channel, predicted at the location of the two spurious unit vectors is of the order of 10^{-3}, which verifies the presence of a stagnation point near the two spurious unit vectors. At $m = 0.55$ (*Fig. 6 (c)*), the corner vortex grows in size and a lip vortex is also formed near the entrant corner. Again, one of the unit vectors near the entrant corner in *Fig. 6 (c)* is in the upstream direction. Similar spurious unit vectors are present near the entrant corner in some of the plots in *Figs. 11* and *16*. It has been verified that the magnitude of the velocity corresponding to such spurious unit vectors near the point where the lip vortex comes in contact with the wall is always smaller than the computational accuracy of the simulation. A further increase in the value of m results in a significant growth of the lip vortex. The corner vortex also grows in size; however, the vortices remain separate with two different centers of recirculation. At $m = 0.6$ and above, the two vortices coalesce together. At $m = 0.6$, the center of recirculation is close to that of the lip vortex. As the elongational power-law index is further increased, the recirculating vortex grows significantly and the center of recirculation moves away from the entrant corner. For $n = 0.25$, $e_0 = e_1 = 0.001\ s^{-1}$ and $\dot{\gamma}_{av} = 1s^{-1}$, the entrance flow simulation converged up to $m = 0.75$, which corresponds to $Tr = 251$ (see **Appendix**). Even though the numerical simulation did not diverge, it failed to converge for $m > 0.75$. In fact for these values of n, e_0, e_1 and $\dot{\gamma}_{av}$, the numerical simulation failed to converge for $m > 0.75$ even for flow in a tube without any contraction. Apparently, at large values of the Trouton ratio, even a small elongational flow due to computational errors in the predicted velocity field for a pure shear flow can give rise to significant elongational stresses. As the elongational stresses due to the error in the predicted velocity field start to dominate the shear stresses, the flow simulation in a tube (with or without a contraction) does not diverge, but fails to converge to a specific value.

For various values of the elongational power-law index, *Fig. 7* shows the velocity along the axis of symmetry. For $m = 0.25$, which corresponds to the truncated power-law model for a purely viscous generalized Newtonian fluid, a slight overshoot (0.56%) is observed in the center-line velocity. This kink in the center-line velocity is maintained as the elongational power-law index is increased, however the kink occurs at a lower normalized velocity and a longer distance is required to reach the fully developed velocity profile.

The normalized pressure variation along the center line for different values of m is shown in *Fig. 8*, where the normalization is with respect to the shear stress at the wall in the downstream channel. The corresponding entrance loss is given in *Fig. 9*. The steep drop in pressure near the abrupt contraction in *Fig. 8*, which corresponds to the entrance loss in *Fig. 9*, is seen to increase significantly with the elongational power-law index. At $m = 0.25$, the predicted entrance loss in terms of the equivalent length of the downstream channel L_e is 1.42, which agrees well with the value reported in the literature (39–43) for a purely viscous generalized Newtonian formulation for power-law model with power-law index $n = 0.25$. The entrance loss increases rapidly with m to a value of $L_e = 29.7$ for $m = 0.75$. *Figure 9* also shows the entrance loss computed by using Binding's approximate analysis (25). In view of various simplifying assumptions in Bindings analysis and the difference in the rheological models at low strain rates, the agreement between the entrance loss predicted by Binding's analytical method and that by finite element flow simulation is quite good. In particular, assuming a slow growth in the radius of the recirculating vortex (R), that is, a large vortex, Binding neglected the terms involving $\left(\frac{dR}{dz}\right)^2$ and $\frac{d^2R}{dz^2}$ in the shear strain rate. However, for the simulations reported in *Fig. 6*, $\frac{dR}{dz}$ for the recirculating vortex is greater than 1. To compare the vortex size predicted by Binding's analysis and that by the finite element flow simulation, *Fig. 10* shows the variation of vortex length (L_v) with power-law index. The

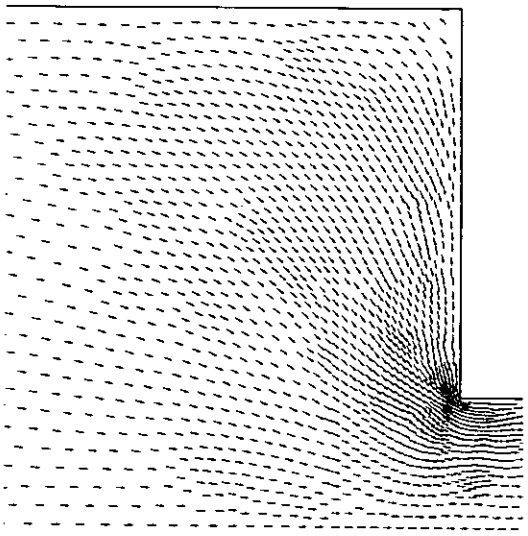

(a)

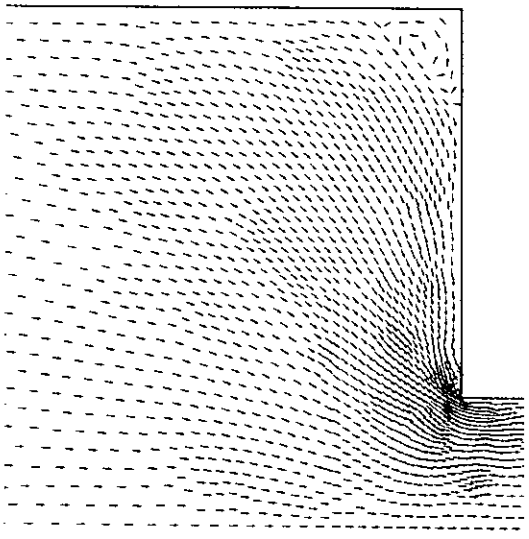

(b)

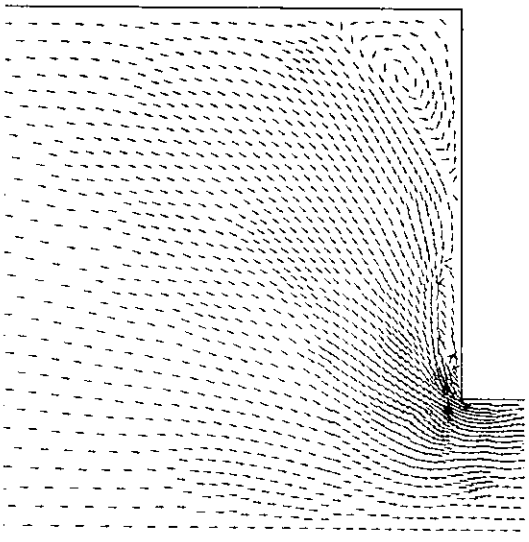

(c)

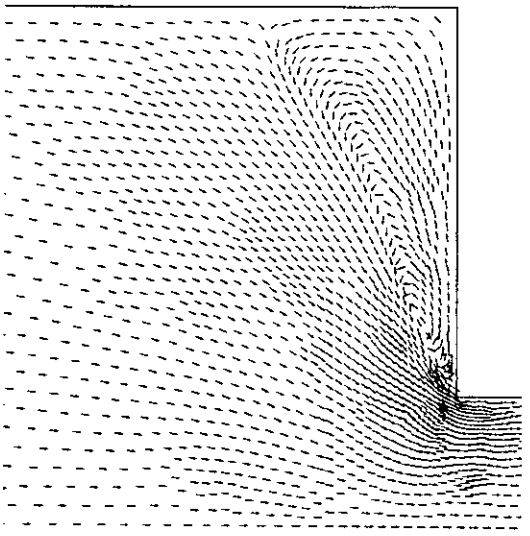

(d)

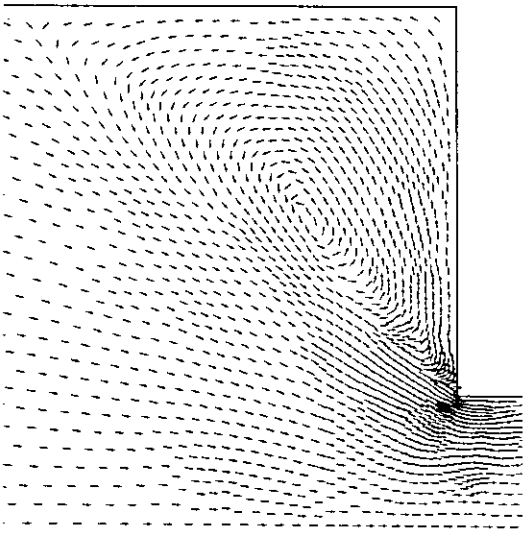

(e)

Fig. 6. Recirculation in 4:1 abrupt contraction for n = 0.25, $e_0 = e_1 = 0.001\ s^{-1}$ and $\dot{\gamma}_{av} = 1\ s^{-1}$. The elongational power-law index, m, is (a) 0.25, (b) 0.5, (c) 0.55, (d) 0.6, (e) 0.75.

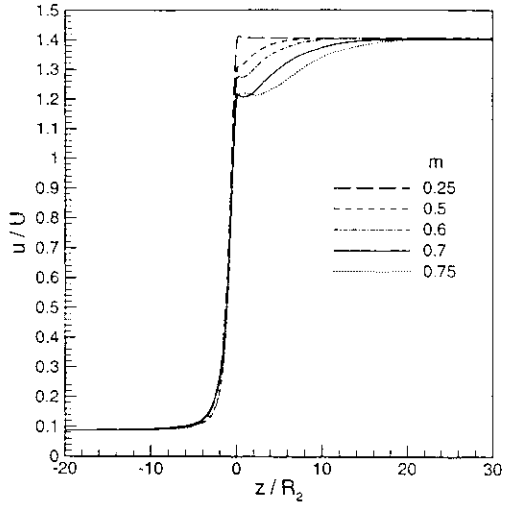

Fig. 7. Velocity along the axis of symmetry for n = 0.25, $e_0 = e_1 = 0.001\ s^{-1}$, $\dot{\gamma}_{av} = 1\ s^{-1}$ and various values of the elongational power-law index.

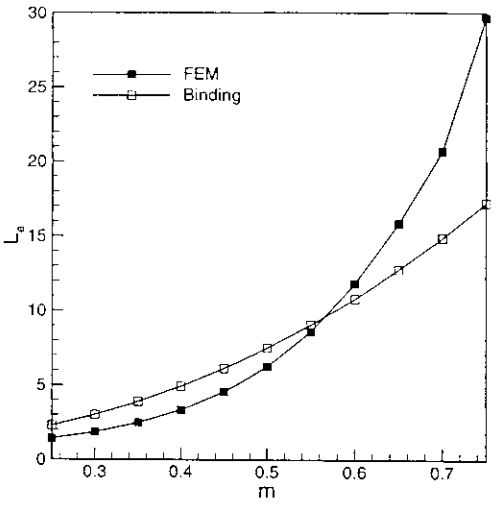

Fig. 9. Entrance loss vs. m for n = 0.25, $e_0 = e_1 = 0.001\ s^{-1}$ and $\dot{\gamma}_{av} = 1\ s^{-1}$.

axial distance between the abrupt contraction and the farthest (from the contraction) node with a positive velocity component in the upstream direction is taken as the vortex length in the finite element simulation. Even though the velocity and pressure field have converged with respect to the mesh refinement (see *Figs. 4* and *5*), depending upon the location of nodes in the finite element mesh, the vortex length was found to change as much as 10% if mesh B in *Fig. 3* is used instead of mesh C. Therefore, in *Fig. 10*, the vortex length predicted by finite element simulation, which has been obtained by using mesh C, may have an error as large as 10%. It is evident from *Fig. 10* that in comparison to the vortex length predicted by finite element flow simulation, Binding's approximate analysis predicts a much larger vortex length. The vortex length in Binding's analysis is actually the length of the upstream channel over which the flow is not fully developed, which is generally much larger than the vortex length.

Effect of Newtonian Limits

For constant values of the shear and elongational power-law indices, a change in the strain rate corresponding to the transition from Newtonian to power-law behavior (e_0 and e_1 in *Eqs 3* and *4*) will affect the value of the Trouton ratio for all strain rates beyond the Newtonian limits. In particular, if the Newtonian limit for elongational viscosity (e_1) is increased with a fixed Newtonian limit for shear viscosity (e_0), the value of the Trouton ratio increases for any strain rate beyond e_1. Therefore, for fixed power-law indices at a

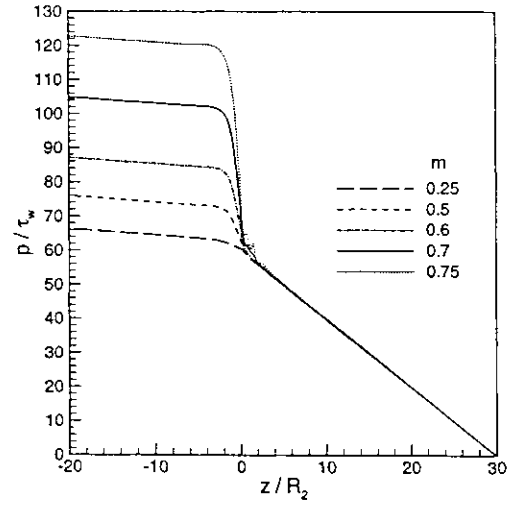

Fig. 8. Pressure along the axis of symmetry for n = 0.25, $e_0 = e_1 = 0.001\ s^{-1}$, $\dot{\gamma}_{av} = 1\ s^{-1}$ and various values of the elongational power-law index.

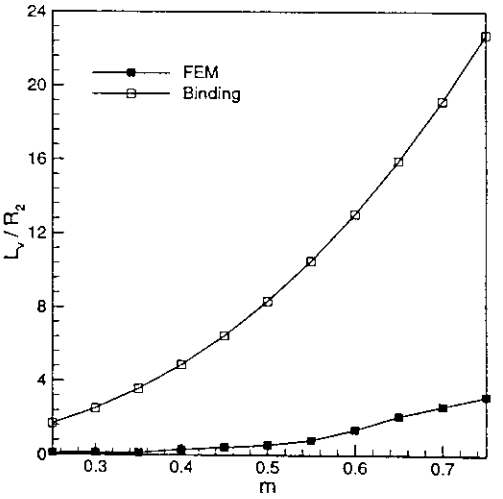

Fig. 10. Vortex length vs. m for n = 0.25, $e_0 = e_1 = 0.001\ s^{-1}$ and $\dot{\gamma}_{av} = 1\ s^{-1}$.

constant flow rate, as e_1 is increased, the recirculating vortex and entrance loss in a channel with abrupt contraction are expected to increase. It should be noted that a change in e_1 will also affect the value of B in *Eq 4*. For power-law indices $n = 0.25$, $m = 0.5$, average strain rate in the downstream channel $\dot{\gamma}_{av} = 1 s^{-1}$, and Newtonian limits $e_0 = e_1 = 0.001\ s^{-1}$, a small corner vortex is predicted, as is seen in *Fig. 6 (b)*. Keeping all other parameters the same as those for *Fig. 6 (b)*, as the Newtonian limit for elongational viscosity (e_1) is increased to $0.003\ s^{-1}$, as shown in *Fig. 11 (a)*, a lip vortex is predicted near the entrant corner and the size of the corner vortex increases significantly. A further increase in e_1 to $0.005\ s^{-1}$ (*Fig. 11 (b)*) not only enhances the lip and corner vortices, but a third intermediate vortex is predicted between the lip and corner vortices. The intermediate vortex could not be captured if a coarse mesh (mesh A or B in *Fig. 3*) is used for the simulation. To eliminate the possibility of the intermediate vortex being a numerical artifact, for the same shear and elongational viscosity parameters as those for *Fig. 11 (b)*, the 4:1 entrance flow was simulated by using two successive refinements of mesh C in *Fig. 3*. The intermediate vortex was evident in the simulations with the finer finite element meshes. This intermediate vortex is predicted only for a narrow range of e_1. As e_1 is increased to $0.006\ s^{-1}$ or decreased to $0.004\ s^{-1}$, the intermediate vortex disappears and only the lip and corner vortices are formed. Since the intermediate vortex is predicted for an extremely narrow range of e_1, it would probably be difficult to capture experimentally. The author is

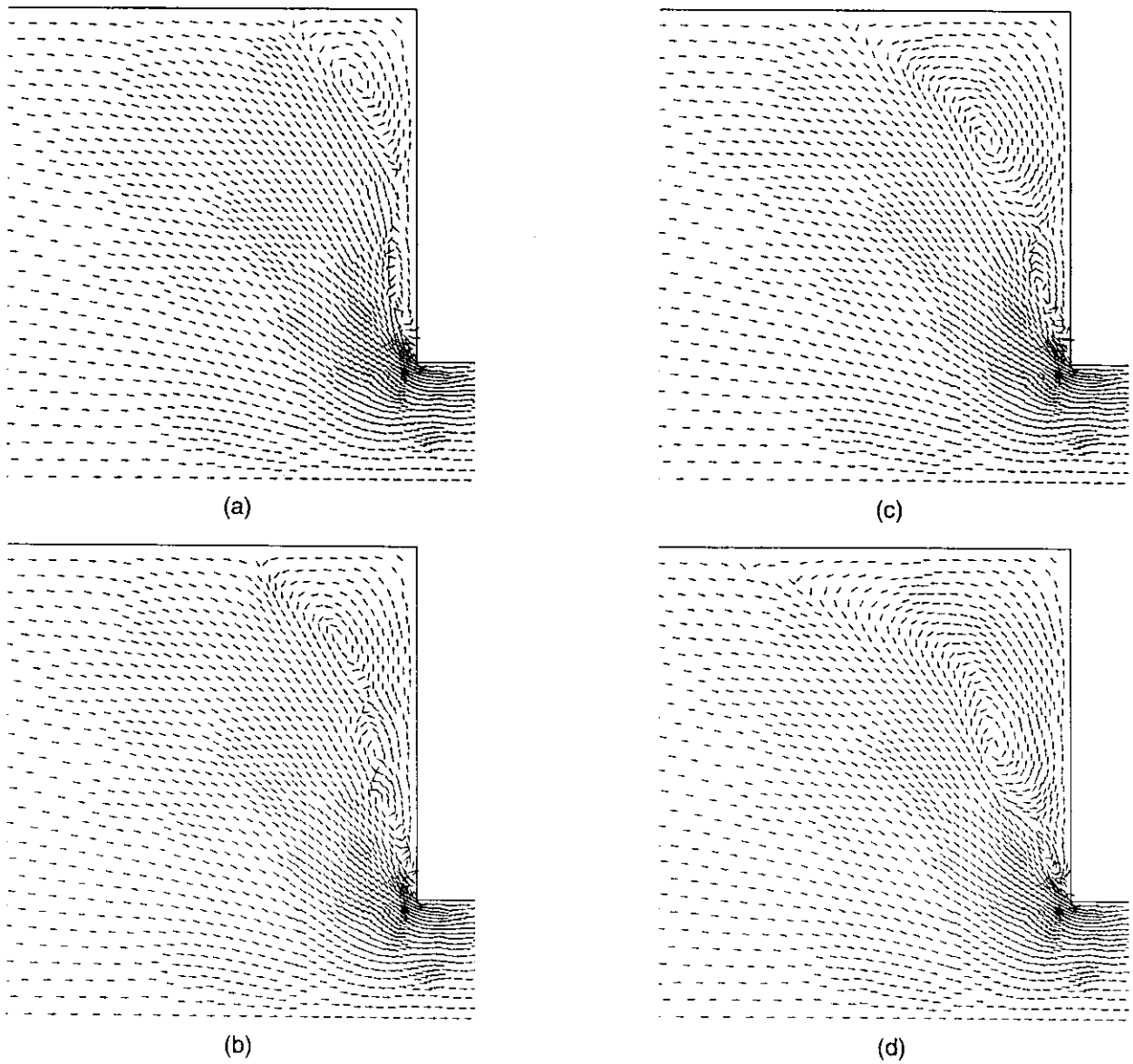

Fig. 11. Recirculation in 4:1 abrupt contraction for $n = 0.25$, $m = 0.5$, $e_0 = 0.001\ s^{-1}$ and $\dot{\gamma}_{av} = 1\ s^{-1}$. The elongational Newtonian limit, e_1, is (a) 0.003, (b) 0.005, (c) 0.01, (d) 0.03 s^{-1}.

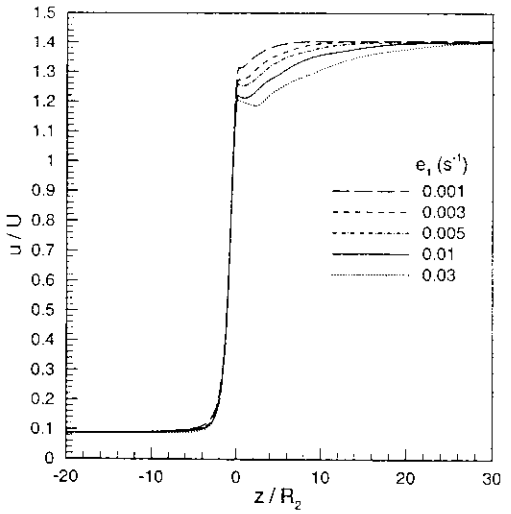

Fig. 12. Velocity along the axis of symmetry for n = 0.25, m = 0.5, e_0 = 0.001 s^{-1}, $\dot{\gamma}_{av}$ = 1 s^{-1} and various values of e_1.

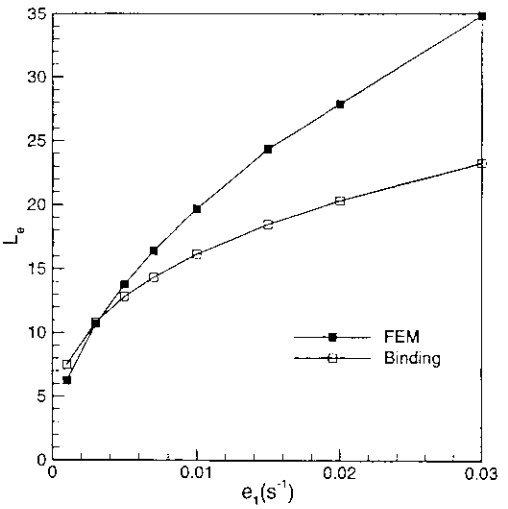

Fig. 14. Entrance loss vs. e_1 for n = 0.25, m = 0.5, e_0 = 0.001 s^{-1} and $\dot{\gamma}_{av}$ = 1 s^{-1}.

not aware of any previous reporting of such an intermediate vortex in the literature for 4:1 entrance flow of polymeric fluids. For e_1 = 0.01 s^{-1}, in *Fig. 11 (c)* the corner vertex is predicted to grow significantly, with only a limited growth in the lip vortex. As e_1 is increased beyond 0.01 s^{-1}, further growth is predicted in the corner vortex, whereas the lip vortex continues to shrink. For e_1 = 0.03 s^{-1} (*Fig. 11 (d)*), the lip vortex is restricted to a small region near the entrant corner. For $e_1 > 0.03$ s^{-1}, the simulation does not converge.

For various values of e_1, with all other parameters fixed, *Fig. 12* shows the velocity along the axis of symmetry. Similar to the effect of an increase in m on the center-line velocity (*Fig. 7*), as e_1 is increased the simulation indicates that the kink in the center-line velocity occurs at a lower normalized velocity and a longer distance is required for the velocity profile to develop completely in the downstream channel. At e_1 = 0.01 and 0.03 s^{-1}, a slight waviness is found in the center-line velocity. These minor fluctuations in the center-line velocity at higher e_1, are more pronounced for the coarse mesh (A in *Fig. 3*) and decrease successively with the finer meshes B and C. As mentioned before, the results in *Fig. 12* have been obtained by using Mesh C.

For various values of e_1, the pressure variation along the axis of symmetry and the corresponding entrance loss are shown in *Figs. 13* and *14*, respectively. Besides a fluctuation in the center-line pressure near the abrupt contraction, at higher values of e_1, a slight waviness is predicted in the center-line pressure in the downstream channel, as indicated in *Fig. 13*. This

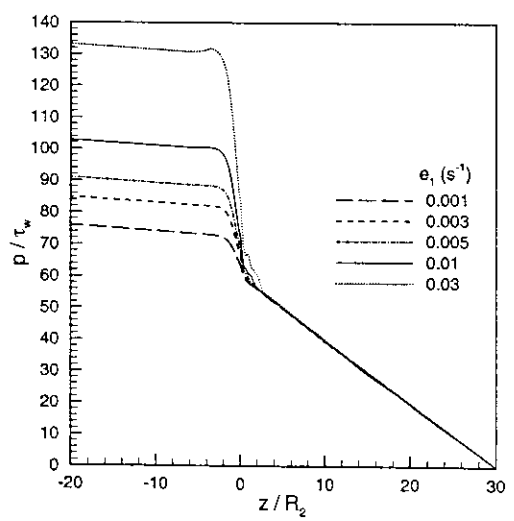

Fig. 13. Pressure along the axis of symmetry for n = 0.25, m = 0.5, e_0 = 0.001 s^{-1}, $\dot{\gamma}_{av}$ = 1 s^{-1} and various values of e_1.

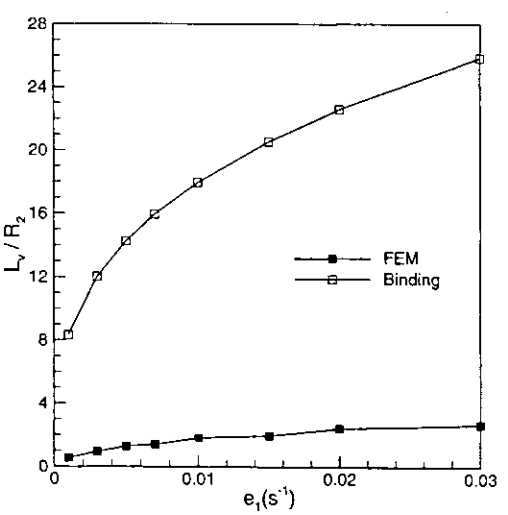

Fig. 15. Vortex length vs. e_1 for n = 0.25, m = 0.5, e_0 = 0.001 s^{-1} and $\dot{\gamma}_{av}$ = 1 s^{-1}.

waviness in the center-line pressure at e_1 = 0.01 and 0.03 s^{-1} is probably related to the waviness in the center-line velocity at the same values of e_1 in *Fig. 12*. Since the Trouton ratio increases as e_1 is increased (see **Appendix**), the entrance loss increases rapidly with e_1. The entrance loss calculated by using Binding's approximate analysis, which is also shown in *Fig. 14*, is in reasonable agreement with the predictions from the finite element flow simulation. However, the vortex length calculated by Binding's analysis (*Fig. 15*) is much larger than the vortex length predicted by the finite element flow simulation. As mentioned in the last section, the vortex length in Binding's analysis is actually the length of upstream channel over which the flow is not fully developed, which is generally much larger than the vortex length.

Effect of Flow Rate

If all the parameters for the shear and elongational viscosities are fixed and the power-law index for elongational viscosity is larger than that for the shear viscosity, then for $e_{II} > e_1$, the value of the Trouton ratio increases with strain rate. Therefore, the recirculating vortex and entrance loss in an axisymmetric 4:1 entrance flow are expected to increase with flow rate. For power-law indices n = 0.25, m = 0.5 and Newtonian limits $e_0 = e_1$ = 0.001 s^{-1}, unit vectors along the direction of velocity at various flow rates are shown in *Fig. 16*. For these viscosity parameters, the unit vectors for $\dot{\gamma}_{av}$ = 1 s^{-1} have already been shown in *Fig. 6 (b)*, which indicates that only a small corner vortex is formed. In *Fig. 16 (a)*, a lip vortex is predicted at

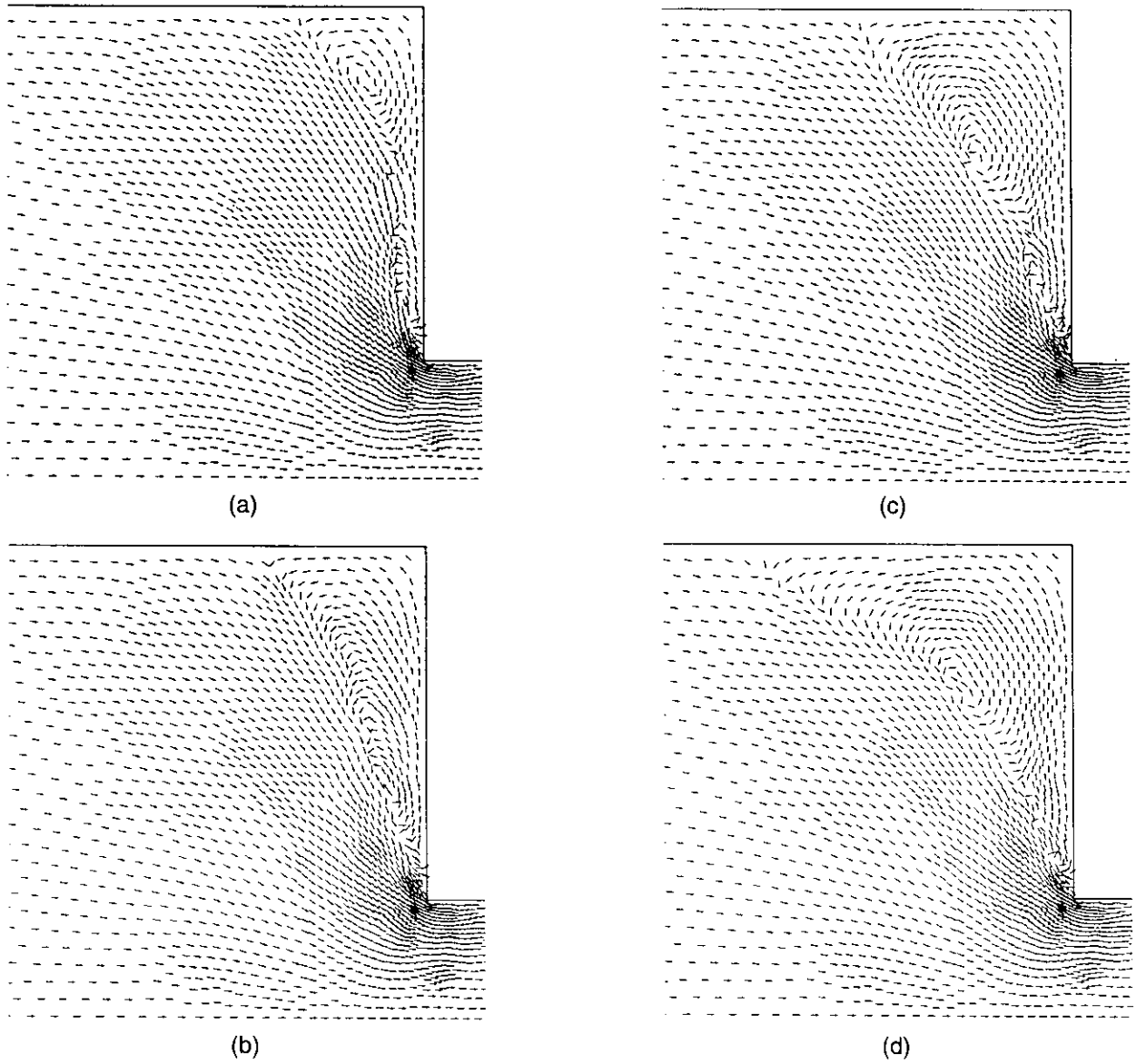

Fig. 16. Recirculation in 4:1 abrupt contraction for n = 0.25, m = 0.5, $e_0 = e_1$ = 0.001 s^{-1}. The average strain rate in the downstream channel, $\dot{\gamma}_{av}$, is (a) 10, (b) 40, (c) 200, (d) 1000 s^{-1}.

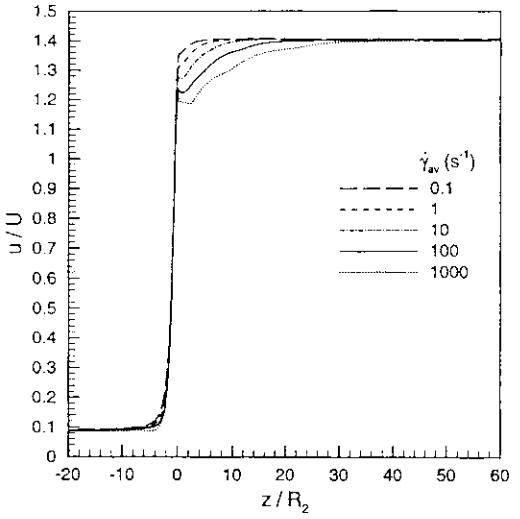

Fig. 17. Velocity along the axis of symmetry for n = 0.25, m = 0.5, $e_0 = e_1 = 0.001\ s^{-1}$ and at various flow rates.

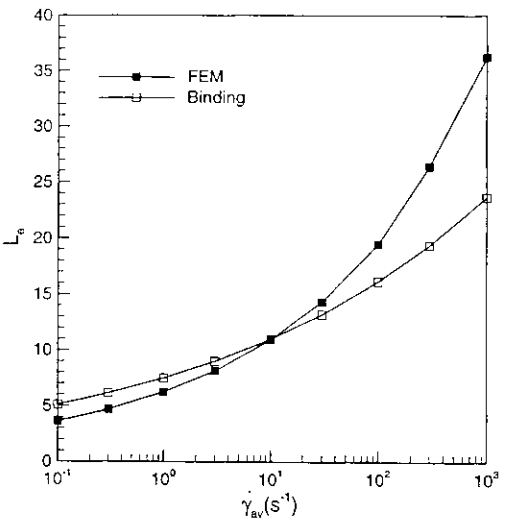

Fig. 19. Entrance loss vs. $\dot{\gamma}_{av}$ for n = 0.25, m = 0.5, $e_0 = e_1 = 0.001\ s^{-1}$.

$\dot{\gamma}_{av} = 10\ s^{-1}$. As the flow rate is increased further to $\dot{\gamma}_{av} = 40\ s^{-1}$ (*Fig. 16 (b)*), the lip vortex is predicted to grow significantly with only a minor growth in the corner vortex. At $\dot{\gamma}_{av} = 40\ s^{-1}$, the simulation indicates that the lip vortex has grown beyond the center of rotation of the corner vortex. However, beyond $\dot{\gamma}_{av} = 40\ s^{-1}$, the predicted corner vortex starts to grow and the lip vortex begins to shrink. At $\dot{\gamma}_{av} = 200\ s^{-1}$ (*Fig. 16 (c)*), the lip and corner vortices are predicted to have distinct centers of rotation. In *Fig. 16 (c)*, the corner vortex has grown significantly, whereas the lip vortex is now limited to a small region near the entrant corner. As $\dot{\gamma}_{av}$ is increased beyond 200 s^{-1}, further growth is predicted in the corner vortex, whereas the lip vortex continues to shrink. At $\dot{\gamma}_{av} = 1000\ s^{-1}$ (*Fig. 16 (d)*), the lip vortex is restricted to a small region near the entrant corner. The simulation does not converge if $\dot{\gamma}_{av}$ is increased beyond 1000 s^{-1}.

For the same shear and elongational viscosity parameters as in *Fig. 16*, the velocity along the axis of symmetry for various flow rates is shown in *Fig. 17*. Similar to the effect of an increase in m and e_1 on the center-line velocity (*Figs. 7* and *12*), the normalized velocity at which the kink occurs in the center-line velocity is predicted to decrease as the flow rate is increased and a longer distance is required for the flow to develop completely in the downstream channel. Since a downstream channel length of more than $30R_2$ is required for the flow to develop completely at $\dot{\gamma}_{av} = 1000\ s^{-1}$, a flow domain with a downstream channel length of $60R_2$ has been used for analyzing the effect of flow rate on the 4:1 entrance flow. Between $z/R_2 = -20$ and $z/R_2 = 30$, the finite-element mesh used in the simulation is the same as mesh C in *Fig. 3*. Additional finite elements have been added between $z/R_2 = 30$ and $z/R_2 = 60$ to increase the length of the

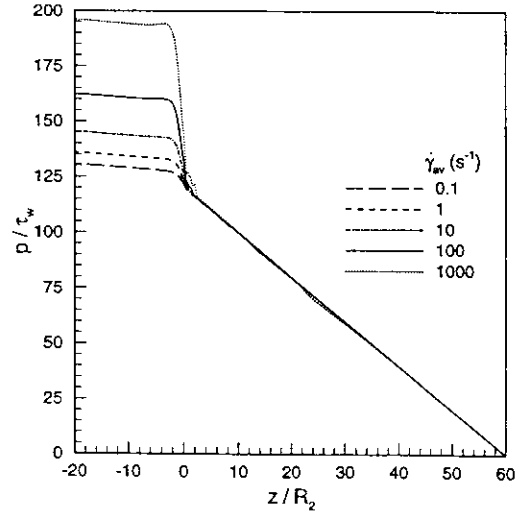

Fig. 18. Pressure along the axis of symmetry for n = 0.25, m = 0.5, $e_0 = e_1 = 0.001\ s^{-1}$ and at various flow rates.

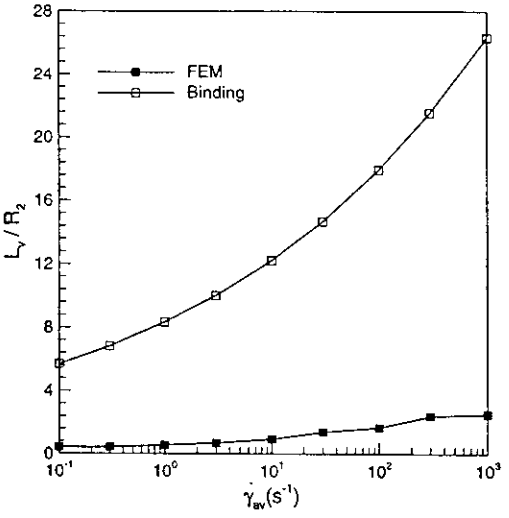

Fig. 20. Vortex length vs. $\dot{\gamma}_{av}$ for n = 0.25, m = 0.5 and $e_0 = e_1 = 0.001\ s^{-1}$.

flow domain. At $\dot{\gamma}_{av}$ = 100 and 1000 s^{-1}, the center-line velocity in the downstream channel has a slight waviness, which is more pronounced for the coarse finite element mesh (A in *Fig. 3*) and decreases as the mesh is refined (meshes B and C in *Fig. 3*).

Figures 18 and *19*, respectively, show the pressure along the axis of symmetry and the corresponding entrance loss at various flow rates. The predicted center-line pressure at $\dot{\gamma}_{av}$ = 100 and 1000 s^{-1} exhibits some fluctuation near the abrupt contraction and a slight waviness is evident in the pressure in the downstream channel. The waviness in the center-line velocity (*Fig. 17*) and pressure (*Fig. 18*) at $\dot{\gamma}_{av}$ = 100 and 1000 s^{-1} are probably correlated. The simulation indicates that the entrance loss increases rapidly as the flow rate is increased. The entrance loss predicted by Binding's approximate analysis, which is also shown in *Fig. 19*, is in reasonable agreement with the corresponding predictions from the finite element flow simulation. *Figure 20* shows the variation in vortex length as the flow rate is increased. Again, in comparison to the vortex length predicted by finite element flow simulation, Binding's analysis predicts a much larger vortex length.

In closing this section, it should be noted that no marching in the Trouton ratio was required to obtain convergence at the higher values of the Trouton ratio. Even though the program never diverged, fluctuations in velocity and pressure, which were observed at higher e_1 and U in *Figs. 12, 13, 17* and *18*, increased at higher values of the Trouton ratio. Because of these fluctuations in velocity and pressure at higher Trouton ratios, the program did not converge. It is evident from *Figs. 9, 14* and *19* that the entrance flow simulation always converged if the entrance loss in terms of the equivalent length of the downstream channel, L_e, is less than 30. In the literature (44), for most polymers the experimentally determined entrance loss in terms of L_e is less than 30. It should be noted that this paper addresses the effect of steady state elongational viscosity on entrance flow. The effects of normal stress difference and transient behavior of elongational viscosity, which can also affect the vortices and extra pressure loss in entrance flow, have not been accounted in this work.

CONCLUSIONS

A finite-element software for simulating axisymmetric flow of polymers has been developed. The shear and elongational viscosities of a polymer have been represented by the truncated power-law model with different power-law indices and Newtonian limits for the two viscosities. The finite-element software has been used to simulate the axisymmetric flow in a channel with 4:1 abrupt contraction. For constant values of the shear-viscosity parameters, the effects of power-law index and Newtonian limit of elongational viscosity on the predicted recirculating vortex and extra pressure loss in a 4:1 entrance flow have been analyzed. Keeping the power-law indices and Newtonian limits for the shear and elongation viscosities constant, the effect of flow rate on the entrance flow has also been analyzed. The recirculating vortex and extra pressure loss in an entrance flow are found to increase significantly with the Trouton ratio. The extra pressure loss predicted by finite element flow simulation is in reasonable agreement with the corresponding predictions from Binding's approximate analysis. However, Binding's analysis predicts a much larger vortex length than the vortex length predicted by finite element simulation of entrance flow.

APPENDIX

Value of the Trouton ratio at the downstream channel wall in a 4:1 abrupt contraction:

(a) For n = 0.25, $e_0 = e_1$ = 0.001 s^{-1}, $\dot{\gamma}_{av}$ = 1 s^{-1}

m	0.25	0.35	0.45	0.55	0.65	0.75
Tr	3.0	7.3	17.6	42.7	103.6	251.0

(b) For n = 0.25, m = 0.5, e_0 = 0.001 s^{-1}, $\dot{\gamma}_{av}$ = 1 s^{-1}

$e_1(s^{-1})$	0.001	0.003	0.005	0.01	0.02	0.03
Tr	27.4	47.5	61.4	86.8	122.7	150.3

(b) For n = 0.25, m = 0.5, $e_0 = e_1$ = 0.001 s^{-1}

$\dot{\gamma}_{av}(s^{-1})$	0.1	1	10	100	1000
Tr	15.4	27.4	48.8	86.8	154.3

REFERENCES

1. R. B. Bird, R. C. Armstrong, and O. Hassager, *Dynamics of Polymeric Liquids*, Vol. 1 and 2, John Wiley, New York (1987).
2. C. A. Hieber and S. F. Shen, *J. Non-Newtonian Fluid Mech.*, **7**, 1 (1980).
3. V. W. Wang, C. A. Hieber, and K. K. Wang, *J. Polym. Eng.*, **7**, 21 (1986).
4. H. H. Chiang, C. A. Hieber, and K. K. Wang, *Polym. Eng. Sci.*, **31**, 116 (1991).
5. R. G. Larson, *Constitutive Equations for Polymeric Melts and Solutions*, Butterworths, Boston (1988).
6. R. Keunings, Chapter 9 in *Fundamentals of Computer Modelling for Polymer Processing*, C. L. Tucker, ed., Hanser, Munich (1989).
7. B. Debbaut, J. M. Marchal, and M. J. Crochet, *J. Non-Newtonian Fluid Mech.*, **29**, 119 (1988).
8. D. Rajagopalan, R. C. Armstrong, and R. A. Brown, *J. Non-Newtonian Fluid Mech.*, **36**, 159 (1990).
9. A. Bolch, P. Townsend, and M. F. Webster, *J. Non-Newtonian Fluid Mech.*, **54**, 285 (1994).
10. R. Guenette and M. Fortin, *J. Non-Newtonian Fluid Mech.*, **60**, 27 (1995).
11. B. Purnode and M. J. Crochet, *J. Non-Newtonian Fluid Mech.*, **65**, 269 (1996).
12. M. Gupta, C. A. Hieber, and K. K. Wang, *Int. J. Numer. Meth. Fluids*, **24**, 493 (1997).
13. C. Beraudo, A. Fortin, T. Coupez, Y. Demay, B. Vergnes, and J. F. Aggasant, *J. Non-Newtonian Fluid Mech.*, **75**, 1 (1998).
14. S. C. Xue, N. Phan-Thein, and R. I. Tanner, *J. Non-Newtonian Fluid Mech.*, **74**, 195 (1998).

15. H. M. Luan and H. Schuch, *J. Rheol.*, **33**, 119 (1989).
16. H. M. Luan, in *Rheology*, Vol. 2, pp. 419–24, G. Astarita, G. Marrucci, and L. Nicolais, eds., Plenum, New York (1980).
17. H. Munstedt and H. M. Luan, *Rheol. Acta*, **20**, 211 (1981).
18. J. A. van Aken and H. Janeschitz-Kriegl, *Rheol. Acta*, **19**, 744 (1980); **21**, 388 (1982).
19. J. F. Stevenson, *AICHE J.*, **18**, 540 (1972).
20. N. E. Hudson and J. Ferguson, *Trans. Soc. Rheol.*, **20**, 265 (1976).
21. F. N. Cogswell, *Polym. Eng. Sci.*, **12**, 64 (1972).
22. A. G. Gibson and G. A. Williamson, *Polym. Eng. Sci.*, **25**, 968 and 980 (1985).
23. T. H. Kwon, S. F. Shen, and K. K. Wang, *Polym. Eng. Sci.*, **26**, 214 (1986).
24. A. G. Gibson, Chapter 3 in *Rheological Measurements*, A. A. Collyer and D. W. Clegg, eds., Elsevier Applied Science (1988).
25. D. M. Binding, *J. Non-Newtonian Fluid Mech.*, **27**, 173 (1988).
26. M. Gupta, C. A. Hieber, and K. K. Wang, *SPE ANTEC Tech. Papers*, **41**, 774 (1995).
27. M. E. Mackay and G. Astarita, *J. Non-Newtonian Fluid Mech.*, **70**, 219 (1997).
28. M. A. Zirnsak and D. V. Boger, *J. Non-Newtonian Fluid Mech.*, **79**, 105 (1998).
29. D. M. Binding, M. A. Couch, and K. Walters, *J. Non-Newtonian Fluid Mech.*, **79**, 137 (1998).
30. D. V. Boger, *Annu. Rev. Fluid Mech.*, **19**, 157 (1987).
31. S. A. White, A. D. Gotsis, and D. G. Baird, *J. Non-Newtonian Fluid Mech.*, **24**, 121 (1987).
32. R. E. Evan and K. Walters, *J. Non-Newtonian Fluid Mech.*, **20**, 11 (1986).
33. R. E. Evan and K. Walters, *J. Non-Newtonian Fluid Mech.*, **32**, 95 (1989).
34. K. Walters and M. F. Webster, *Philos. Trans. R. Soc. London A*, **308**, 199 (1982).
35. K. Walters and D. M. Rawlinson, *Rheol. Acta*, **21**, 547 (1982).
36. D. M. Binding and K. Walters, *J. Non-Newtonian Fluid Mech.*, **30**, 233 (1988).
37. J. Azaiez, R. Guenette, and A. Ait-Kadi, *J. Non-Newtonian Fluid Mech.*, **62**, 253 (1996).
38. L. M. Quinzani, R. A. Brown, and R. C. Armstrong, *J. Non-Newtonian Fluid Mech.*, **52**, 1 (1994).
39. D. V. Boger, R. Gupta, and R. I. Tanner, *J. Non-Newt. Fluid Mech.*, **4**, 239 (1978).
40. M. E. Kim-E, R. A. Brown, and R. C. Armstrong, *J. Non-Newt. Fluid Mech.*, **13**, 341 (1983).
41. E. Mitsoulis, J. Vlachopoulos, and F. A. Mirza, *Polym. Eng. Sci.*, **24**, 707 (1984).
42. C. A. Hieber, *Rheol. Acta*, **26**, 92 (1987).
43. M. Gupta, C. A. Hieber, and K. K. Wang, *Polym. Eng. Sci.*, **34**, 209 (1994).
44. C. A. Hieber (Chapter 1), A. I. Isayev, and R. K. Upadhyay (Chapter 2), in *Injection and Compression Molding Fundamentals*, A. I. Isayev, ed., Marcel Dekker (1987).